Acta Pharmaceutica Sinica B 2025;15(5):2746−2763

Chinese Pharmaceutical Association
Institute of Materia Medica, Chinese Academy of Medical Sciences

Acta Pharmaceutica Sinica B

www.elsevier.com/locate/apsb
www.sciencedirect.com

ORIGINAL ARTICLE

Prodrug-based combinational nanomedicine remodels lipid metabolism for reinforced ferroptosis and immune activation

Ling Lin[a,†], Zaixiang Fang[a,†], Guohao Liu[a], Yiwei Liu[a], Zhiqian Li[a], Dayi Pan[a], Yunkun Li[a], Hemi Kang[b], Xiaoding Shen[a], Jingyao Zhang[a], Qiyong Gong[a,c,d,*], Kui Luo[a,c,*], Jing Jing[a,*]

[a]*Department of Radiology, Huaxi MR Research Center (HMRRC), Institution of Radiology and Medical Imaging, Breast Center, Institute of Breast Health Medicine, State Key Laboratory of Biotherapy, Core Facilities, West China Hospital, Sichuan University, Chengdu 610041, China*
[b]*College of Chemical Engineering, Sichuan University, Chengdu 610041, China*
[c]*Functional and Molecular Imaging Key Laboratory of Sichuan Province, NHC Key Laboratory of Transplant Engineering and Immunology, Research Unit of Psychoradiology, Chinese Academy of Medical Sciences, Chengdu 610041, China*
[d]*Xiamen Key Lab of Psychoradiology and Neuromodulation, Department of Radiology, West China Xiamen Hospital of Sichuan University, Xiamen 361021, China*

Received 9 December 2024; received in revised form 15 February 2025; accepted 20 February 2025

KEY WORDS

Prodrug-based nanomedicines;
Ferroptosis;
Lipid metabolism;
Immune activation;
Breast cancer;
Heparin;
Combinational therapy;
ROS-responsiveness

Abstract Ferroptosis is a form of programmed cell death characterized by overwhelmed lipid oxidation, and it has emerged as a promising strategy for cancer therapy. Enhanced ferroptosis could overcome the limitations of conventional therapeutic modalities, particularly in difficult-to-treat tumors. In this study, we developed a dual-modality therapy in nanomedicine by combining paclitaxel (PTX) chemotherapy and pyropheophorbide-a (Ppa) phototherapy. Heparin (HP) was grafted with poly(*N*-(2′-hydroxy) propyl methacrylamide) (pHPMA) using reversible addition−fragmentation chain transfer polymerization to form HP-pHPMA (HH), which was utilized to deliver Ppa and PTX, yielding HP-pHPMA-Ppa (HH-Ppa) and HP-pHPMA-PTX (HH-PTX), respectively. The prodrug-based combinational nanomedicine (HH-PP) was formed by co-assembly of HH-PTX and HH-Ppa. It was found that HH-PP treatment significantly disrupted lipid metabolism in triple-negative breast cancer (TNBC) cells, induced extensive lipid oxidation, and promoted ferroptosis. *In vivo*, HH-PP intervention achieved a tumor growth inhibition

*Corresponding authors.
E-mail addresses: qiyonggong@hmrrc.org.cn (Qiyong Gong), luokui@scu.edu.cn (Kui Luo), jingjing@wchscu.edu.cn (Jing Jing).
[†]These authors made equal contributions to this work.

Peer review under the responsibility of Chinese Pharmaceutical Association and Institute of Materia Medica, Chinese Academy of Medical Sciences.

https://doi.org/10.1016/j.apsb.2025.03.016

rate of 86.63% and activated adaptive immunity with an elevated $CD8^+$ cytotoxic T cell infiltration level. This combinational nanomedicine offers a promising platform for co-delivery of multiple therapeutic agents. It exerts a promising anti-tumor effect *via* enhanced ferroptosis and ferroptosis-induced immune activation by disrupting lipid metabolism in TNBC cancer cells.

1. Introduction

Ferroptosis, also known as "iron death", is a form of programmed cell death, and it could be a promising strategy for cancer therapy[1,2]. Ferroptosis inducers have been reported to suppress tumor growth, reshape the tumor microenvironment, and enhance immunotherapy responses to overcome resistance to conventional therapies in various tumors[3,4]. Treatment with ferroptosis inducers is imperative for aggressive tumors that are difficult to treat, such as triple-negative breast cancer (TNBC)[5,6]. Beyond its direct cytotoxic effect, ferroptosis can promote immunogenic cell death (ICD) and invigorate the immune system by inducing the release of damage-associated molecular patterns (DAMPs), presenting antigens to dendritic cells (DCs) to form mature ones, activating immune cells proliferation[7]. The immune activation process, stimulated by adaptive immune response, could lead to recognition and attack of tumor cells[8]. It is particularly important in "cold" tumors, including TNBC, which have a low level of immunogenicity and poor immune cell infiltration[9,10].

Although TNBC cells are susceptible to ferroptosis compared to conventional chemotherapies, several challenges exist to inducing ferroptosis and destroying tumors effectively[11,12]. Ferroptosis is triggered by overwhelmed lipid oxidation, which is influenced by lipid metabolic properties and is governed by intracellular redox balance[13]. Multiple intracellular reductive systems, represented by the glutathione peroxidase 4 (GSH/GPX4) pathway, could defend against oxidative stress and maintain redox balance[14]. Attacking one therapeutic target by affecting certain antioxidants or intervening in the metabolism might not sufficiently disrupt the redox balance, resulting in insufficient lipid oxidation and incomplete ferroptosis in tumor tissues[15]. The remaining tumor cells may recover and migrate into the circulation, leading to tumor migration and invasion[16,17]. Therefore, combination therapies with two or more therapeutic agents may simultaneously modulate metabolism, increase oxidative lipid levels, and exert synergistic pharmacological actions to enhance ferroptosis.

Paclitaxel (PTX), a first-line chemotherapeutic agent for treating TNBC, is known for disrupting microtubule dynamics and inhibiting cell mitosis[18]. It has also been shown to modulate metabolic processes and induce ferroptosis when combined with other therapeutic modalities, thereby increasing the anticancer sensitivity of these combination treatment modalities against TNBC cells[19,20]. In addition, pyropheophorbide-a (Ppa), a photodynamic therapy (PDT) agent, generates reactive oxygen species (ROS) upon light irradiation, effectively exerting oxidative stress in tumor cells, which is a critical trigger of ferroptosis[21,22]. Therefore, combining Ppa and PTX may be a promising synergistic approach to induce ferroptosis in TNBC cells and activate adaptive immune responses in TNBC tissues.

Nevertheless, the combinational use of small molecular compounds for clinical application is constrained by several issues, including low solubility, poor tumor targeting, and high systemic toxicity[23,24]. For these concerns, novel biomaterials have been developed to serve as efficient drug carriers for delivering Ppa and/or PTX[25-27]. Although natural polysaccharides such as heparin (HP) have advantageous biological properties, they are inherently inadequate as stand-alone drug carriers[28,29]. Consequently, enhancing the functionality of natural polysaccharide through modification has emerged as a reliable strategy. One strategy is to graft hydrophilic and biocompatible polymers onto HP, effectively transforming HP into a versatile nanocarrier for co-delivery of multiple therapeutic agents[30,31]. Poly(*N*-(2′-hydroxy) propyl methacrylamide) (pHPMA) is a hydrophilic polymer with high biocompatibility and has been widely investigated as a substituent group in a drug delivery carrier[32]. This approach not only improves the solubility and bioavailability of therapeutic agents but also enhances their targeting efficiency to tumor tissues, thus facilitating the co-delivery of drugs in a combination nanomedicine for tumor treatment[33].

In this study, we grafted pHPMA onto HP to produce HP-pHPMA (HH) *via* reversible addition−fragmentation chain transfer (RAFT) polymerization. HH was employed to deliver a photosensitizer, Ppa, to yield HP-pHPMA-Ppa (HH-Ppa) and an anti-tumor drug, PTX, to yield HP-pHPMA-PTX (HH-PTX). The co-assembly of HH-PTX and HH-Ppa resulted in forming a prodrug-based combinational nanomedicine, HH-PP (Scheme 1). Upon penetration into tumor tissues and accumulation in tumor cells, ROS generated by Ppa in HH-PP under laser irradiation-induced cell death and promoted the release of PTX. HH-PP was also found to significantly affect lipid metabolism, as evidenced by decreased GSH and GPX4 and increased levels of oxidized phosphatidylethanolamine (oxPE) and other oxidative lipids. The disruption of lipid homeostasis markedly enhanced ferroptosis in tumor cells, thereby activating an adaptive immune response. HH-PP treatment yielded an encouraging tumor growth inhibition rate in a tumor-bearing animal model.

2. Materials and methods

2.1. Materials, cell lines and animals

All chemicals used were of analytical grade, and their sources were listed in Supporting Information 1.1. Instruments were shown in Supporting Information 1.2. Trackers and probes, except specifically mentioned ones, were obtained from Beyotime Biotechnology (Chengdu, China), and antibodies were purchased from BD Pharmingen (Shanghai, China). BODIPY 581/591 C11 were obtained from Jiqi Biotechnology (Shanghai, China). Cells were purchased from the Chinese Academy of Science Cell Bank (Shanghai, China). Mice and nude mice (female, 6−8 weeks) were purchased from Gem Pharmatech (Chengdu, China). All

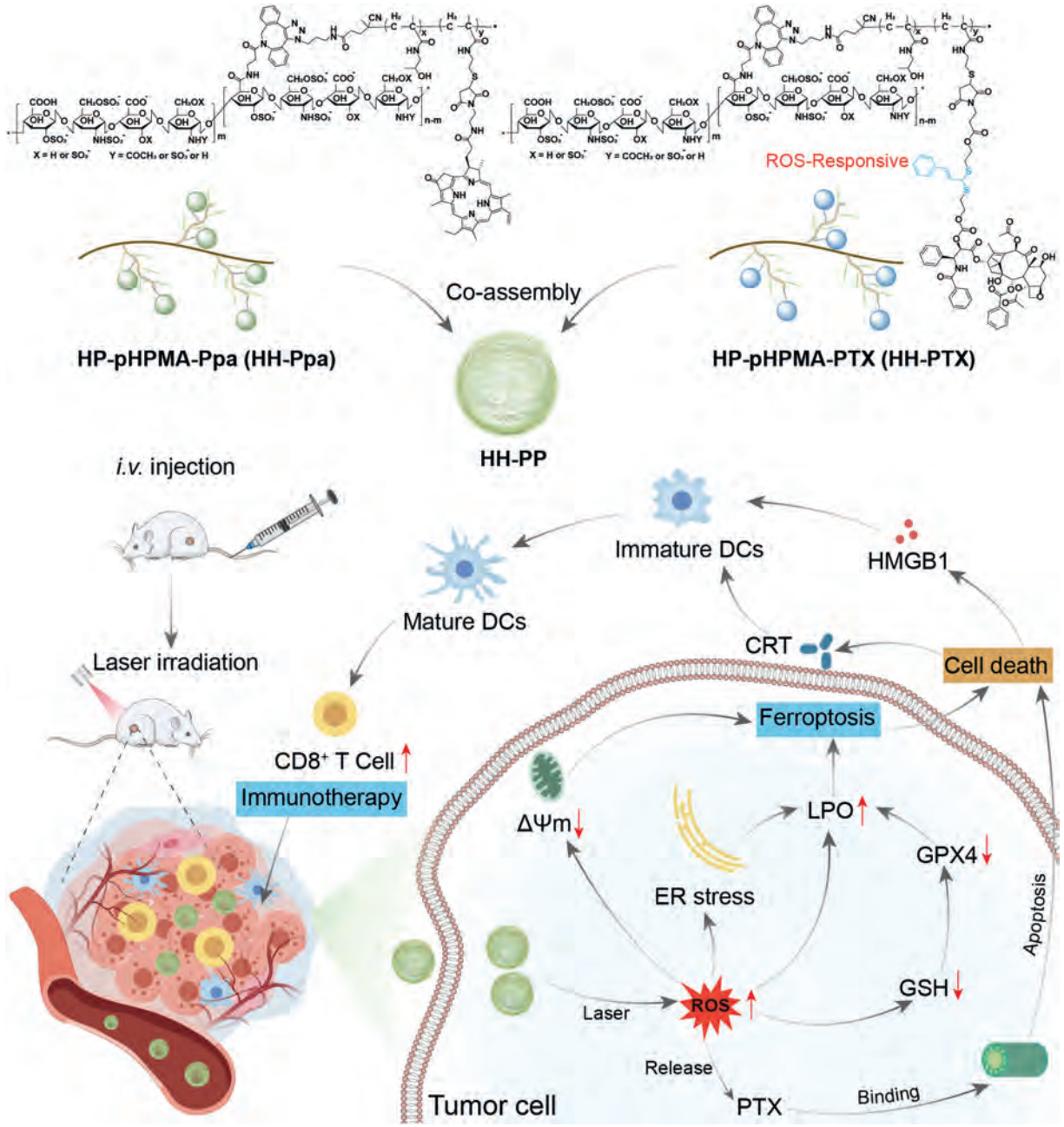

Scheme 1 Schematic illustration of the structures of HH-Ppa, HH-PTX, and HH-PP and the mechanism of inducing ferroptosis and stimulating immune activation by HH-PP.

experimental procedures were executed according to the protocols approved by the Animal Ethics Committee of West China Hospital of Sichuan University (No. 20220602003).

2.2. *Synthesis and characterization of compounds and polymers*

The synthesis routes are shown in Supporting Information 1.3. Briefly, the macromolecular chain transfer agent, HP-CTA, was synthesized from HP-DBCO and CTA-N_3. HP-CTA, together with *N*-(2′-hydroxyl)-propyl methyl propylene amide (HPMA), and 2-propenamide, 2-methyl-*N*-[2-(2-pyridinyldithio)ethyl] (MA−SS−Py) were used to form HH which was subsequently employed to produce HP-pHPMA-SH (HH-SH). HH-SH was introduced to form HH-Ppa and HH-PTX when it reacted with Mal-Ppa and Mal-CA-TA-PTX, respectively. Reaction products were characterized *via* the following measurements, including NMR spectra, HRMS, LC−MS analysis, GPC analysis, DSC analysis, or FTIR analysis, and details were exhibited in Supporting Information 1.4.

2.3. *Preparation and characterization of nanoparticles*

HH-PTX and HH-Ppa were dissolved in deionized water and prepared using an ultrasound machine. Co-assembled HH-PP from HH-PTX and HH-Ppa at different ratios were prepared by physically mixing HH-Ppa and HH-PTX at a high concentration of

100 mg/mL, dispersing them in deionized water and then subjecting to ultrasonic treatment. For HH-PTX imaging, 5-carboxy-x-rhodamine(Rox)-labeled HH-PTX was prepared, named ^{Rox}HH-PTX, and its co-assembled HH-PP was renamed ^{Rox}HH-PP.

Characterizations of the nanoparticles include size and zeta potential measurements, morphology observation, *in vitro* stability and photostability evaluation, and *in vitro* singlet oxygen production assessment. General measurement methods and instruments were listed in Supporting Information 1.5.

2.4. Cellular uptake

Mouse breast cancer cells (4T1 cells) were cultured in Roswell Park Memorial Institute (RPMI-1640) with 10% fetal bovine serum (FBS) (*v*/*v*), 100 U/mL penicillin G, and 100 μg/mL streptomycin at 37 °C under 5% CO_2. Cells (2×10^3) were treated with different nanoparticles for 24 h (^{Rox}HH-PTX, HH-Ppa, ^{Rox}HH-PP) (Ppa: 1 μg/mL, and PTX: 1.4 μg/mL). After incubating with cell organelle-specific trackers and staining with Hoechst 33,342, fluorescence images of organelles, Rox, Ppa, and cell nuclei were captured by confocal laser scanning microscopy (CLSM).

2.5. Cell toxicity studies

In vitro experiments were conducted in the following groups: Ppa and PTX without irradiation (Ppa + PTX), free Ppa and free PTX with irradiation (Ppa + PTX + L), HH-PTX, HH-Ppa, HH-Ppa with irradiation (HH-Ppa + L), HH-PP, and HH-PP with irradiation (HH-PP + L). 4T1 cells (2×10^4) were co-cultured with different nanoparticles for 24 h (Ppa: 2 μg/mL, and PTX: 2.8 μg/mL). Subsequently, the HH-Ppa + L and HH-PP + L groups underwent irradiation (1 J/cm^2, 660 nm, 16 mW/cm^2, 62 s) and then incubated for another 6 h. After incubation, cells were sampled for the following analyses. For live and dead viability, cells were treated with a live and dead cell viability kit, and their images were captured under a microscope. Cells were fixed with 4% polyformaldehyde and incubated with Hoechst 33,342 and actin and tubulin trackers to assess the impact of nanoparticles on microtubules and microfilaments. Cellular microtubule and microfilament morphologies were captured under CLSM. For assessing intracellular ROS generation and measuring the mitochondria membrane potential, cells were co-cultured with 2,7-dichlorodihydrofluorescein diacetate (DCFH-DA), and 5,5′,6,6′-tetrachloro-1,1′,3,3′-tetraethyl-imidacarbocyanine iodide (JC-1), respectively. The fluorescence images of ROS or JC-1 were acquired with an inverted fluorescence microscope or CLSM. Cells were harvested for semi-quantification analysis with flow cytometry.

2.6. TEM imaging

4T1 cells (1×10^8) were treated with HH-Ppa, HH-PTX or HH-PP for 24 h (Ppa: 2 μg/mL, and PTX: 2.8 μg/mL), and the cells in the HH-Ppa + L and HH-PP + L groups were irradiated under 660 nm laser (1 J/cm^2, 16 mW/cm^2, 62 s), following with incubation for another 1 h. Cells were collected and fixed with 2.5% glutaraldehyde. Subsequently, they were sectioned by a slicer to obtain bio-TEM images.

2.7. Lipid oxidation analysis and ferroptosis-related assays

4T1 cells (2×10^5) were subjected to the same treatment in 2.5. The concentrations of malondialdehyde (MDA), GSH, and lactate dehydrogenase (LDH) were assessed using an MDA kit, a GSH assay kit, and an LDH assay kit, respectively. The results were normalized based on the cell number according to the manufacturer's instructions. Cells were stained with BODIPY 581/591 C11 for lipid oxidation analysis and Hoechst 33,342. Cells were harvested for semi-quantification analysis with flow cytometry, and their images were acquired using CLSM.

2.8. Untargeted lipidomic study

4T1 cells (1×10^{10}) were treated similarly in 2.6. Lipids were collected and prepared according to the previous report[34]. Instrument parameters were shown in Supporting Information 1.8. The raw data were acquired on HPLC−MS/MS, and lipids were extracted and identified *via* MS-DIAL software ($n = 5$).

2.9. Mouse model construction and in vivo biodistribution

Xenograft tumors were generated by subcutaneous injection of 4T1 cells (50 μL, 1×10^7/mL) into the right posterior backs of the Balb/c nude mice. Tumor-bearing mice were randomized into five groups (Saline, Ppa + Rox, ^{Rox}HH-PTX, HH-Ppa, ^{Rox}HH-PP; Ppa: 5 mg/kg, Rox: 0.49 mg/kg; $n = 4$). When the tumor size reached 100 mm^3, these mice were injected with different formulations *via* the tail vein and subjected to living imaging. At 72 h post-injection, their organs were collected for *ex-vivo* imaging after sacrifice. Frozen sections of tumors were prepared, and fluorescence images were captured using CLSM.

2.10. Pharmacokinetics analysis

Female Balb/c mice were randomly divided into four groups, and they were intravenously injected with Ppa + Rox, ^{Rox}HH-PTX, HH-Ppa, or ^{Rox}HH-PP (Ppa: 5 mg/kg, Rox: 0.49 mg/kg; $n = 4$). 20 μL of blood samples from the orbital venous plexus were collected at different time points post-injection. The blood samples were added with 80 μL of H_2O and stored at 4 °C for 24 h. The samples were centrifuged at 3500 rpm for 15 min, and the supernatants were extracted with 300 μL of DMSO. The Ppa and Rox concentrations in the supernatant were measured *via* a microplate reader (Ex: 570 nm, Em: 620 nm for Rox, Ex: 640 nm, Em: 680 nm for Ppa).

2.11. In vitro ICD effect

4T1 cells (1×10^5) were subjected to the same treatment in 2.5. Cells were stained sequentially with high mobility group box 1 (HMGB1) and Hoechst 33,342. For calreticulin (CRT) staining, these cells were fixed and then stained with an actin tracker and a CRT probe.

2.12. Stimulation of BMDCs maturation

Mouse bone marrow cells collected from mice tibia and femur were cultured in the RPMI medium supplemented with 20 ng/mL human granulocyte-macrophage colony-stimulating factor (GM-CSF). They were stimulated to generate bone marrow DCs (BMDCs) by culturing for 6 days. After 4T1 cells were processed with the same treatment in 2.5, the spent medium from 4T1 cells was added into the BMDCs medium for BMDCs maturation stimulation for 24 h. The level of DC maturation was investigated

with flow cytometry by assessing the portion of $CD80^+CD86^+$ cells in $CD11c^+$ cells ($n = 3$).

2.13. In vivo anti-tumor experiments and biosafety evaluation

Tumor-bearing Balb/c mice were randomized into eight groups, and they received intravenous injections of different formulations presented in 2.5 *via* tail vein on Days 1 and 9 (Ppa: 5 mg/kg, PTX: 7 mg/kg; $n = 5$). After 24 h post-injection, tumors in the Ppa + PTX + L, HH-Ppa + L, HH-PP + L groups were irradiated (96 J/cm^2, 660 nm, 320 mW/cm^2, 5 min). The tumor volume and the mice's body weight were monitored twice daily. Euthanasia was performed if the tumor length exceeded 15 mm or the mice's body weight decreased by more than 20%. After 17 days of treatment, tumors were harvested, and tumor growth inhibition (TGI) rates were calculated from the equation, as shown in Eq. (1):

$$\mathrm{TGI} = 100 - [m_t / m_c \times 100] \quad (1)$$

where m_t is the tumor weight from the treatment group, and m_c is the tumor weight from the control group. The mice's blood was withdrawn for biochemistry analysis. The main organs were stained with H&E, and tumor tissues were subjected to immunohistochemistry (Ki67 and CD31) and immunofluorescence analysis (TUNEL).

2.14. In vivo immune activation study and Oil Red O staining

Tumor tissues from 2.13 were subjected to immunofluorescence analysis (HMGB1, CRT, CD4, and CD8). They were frozenly sectioned, and the tumor frozen slices were stained with Oil Red O after fixing with 10% formaldehyde and rinsing with 60% isopropanol.

2.15. Statistical analysis

Statistical analyses were performed, including one-way ANOVA, unpaired *t*-test, or Tukey's multiple comparison test, using GraphPad Prism 10 software. Data are presented as mean ± standard deviation (SD, *ns*, not significant. $*P < 0.05$. $**P < 0.01$. $***P < 0.001$.). Principal component analysis (PCA) of lipidomes data was performed using the SIMCA 16.0 software (Sartorius AG, Göttingen, Germany). Heat mapping, volcano analysis, and fold change analysis were performed using MetaboAnalyst 4.0 (McGill University, Quebec, Canada).

3. Results and discussion

3.1. Synthesis and characterization

HP was selected as the base polymer to prepare the combinational nanomedicine due to its inherent biocompatibility and versatility for chemical modification. However, native HP has a limited capacity as a drug carrier, and we modified it with pHPMA *via* RAFT polymerization. This modification allows precise control of the molecular weight of the drug carrier and enables the conjugation of therapeutic agents such as Ppa and PTX onto the carrier. As shown in Supporting Information Scheme S1, HH-Ppa and HH-PTX were synthesized through condensation, polymerization, and click reaction (Supporting Information Figs. S1−S9). HP-CTA, a macromolecular chain transfer agent, was synthesized in two steps. In the first step, HP was modified with DBCO-NH_2 to create HP-DBCO according to a previously reported method[35]. Differential scanning calorimetry (DSC) revealed a distinct exothermic peak for HP-DBCO at 229.33 °C, differing from that of native HP (245.56 °C), DBCO-NH_2 (an endothermic peak, 102.83 °C) and a mixture of HP and DBCO-NH_2 (244.83 °C), confirming successful conjugation (Fig. 1A). UV spectra further supported the modification with absorption peaks at 294 and 312 nm for HP-DBCO that were not present in native HP (Supporting Information Fig. S10). Quantitative analysis showed that the content of DBCO-NH_2 in HP-DBCO was 12.68%, which was calculated from a standard curve (Supporting Information Fig. S11).

Subsequently, HP-CTA was synthesized using alkyne and azide groups *via* a copper-free click reaction. ^{1}H nuclear magnetic resonance (^{1}H NMR) spectra confirmed the presence of aromatic protons at 8.0−7.0 ppm, characteristic peaks of the DBCO and CTA groups (Figs. S5−S6). In contrast, Fourier-transform infrared spectra (FTIR) showed the disappearance of the azide peak of CTA-N_3 at 2229.43 cm^{-1}, verifying successful synthesis (Supporting Information Fig. S12). DSC analysis displayed an exothermic peak at 228.00 °C for HP-CTA, indicating a slight shift from HP-DBCO (Fig. 1A). UV absorbance analysis also confirmed a peak at 307 nm, consistent with the spectral properties of CTA (Fig. 1B). The content of CTA in HP-CTA was measured at 9% (Supporting Information Fig. S13).

HH was synthesized by RAFT polymerization using HP-CTA as the chain transfer agent, HPMA as the monomer, and 2,2′-azobis[2-(2-imidazolin-2-yl) propane] dihydrochloride as an initiator under an argon atmosphere. Subsequently, HH-Ppa and HH-PTX were synthesized by conjugating Mal-Ppa[36] and Mal-TA-CA-PTX[37], respectively, to HH through a thiol-maleimide click reaction. The characterization by gel permeation chromatography revealed a slight increase in the molecular weight (Mw) for HH-Ppa and HH-PTX in comparison to HH, which indicated successful conjugation of the drug (Supporting Information Fig. S14, Supporting Information Table S1). ^{1}H NMR analysis confirmed the presence of characteristic peaks for Ppa and PTX, verifying successful synthesis of HH-Ppa and HH-PTX (Figs. S7−S9). The drug loading content (DLC) was measured to be 7.0% for Ppa and 10% for PTX (Supporting Information Fig. S15). To map the distribution of HH-PTX *in vitro* and i*n vivo*, we synthesized rhodamine (Rox)-labeled HH-PTX, ^{Rox}HH-PTX, according to a previous method[37], with a Rox content of 0.7%.

The self-assembly and co-assembly behaviors were investigated, showing the critical aggregation concentrations of HH-Ppa and HH-PTX were determined to be 3.69 μg/mL and 12.23 μg/mL, respectively, indicating that both could form nanoparticles in an aqueous solution (Supporting Information Table S2). Alterations in size, polydispersity index (PDI), and correlation coefficients of HH-Ppa and HH-PTX at varying concentrations *via* dynamic light scattering (DLS) indicated that both HH-Ppa and HH-PTX were capable of maintaining a nanoscale size at a low concentration (Supporting Information Fig. S16, Supporting Information Tables S3 and S4). The particle size and PDI of the co-assembled product formed from HH-Ppa and HH-PTX were further investigated at varying HH-PTX/HH-Ppa ratios. The results showed that a 1:1 mass ratio of HH-PTX to HH-Ppa resulted in an optimal particle size and PDI, and the resulting product, HH-PP (DLC of PTX: 5%; DLC of Ppa: 3.5%), was used for the following *in vitro* and *in vivo* studies (Supporting Information Fig. S17, Supporting Information Table S5). The hydrodynamic diameters of HH-Ppa and HH-PTX were 114.2 ± 6.7 and 150.6 ± 12.2 nm, respectively. In contrast,

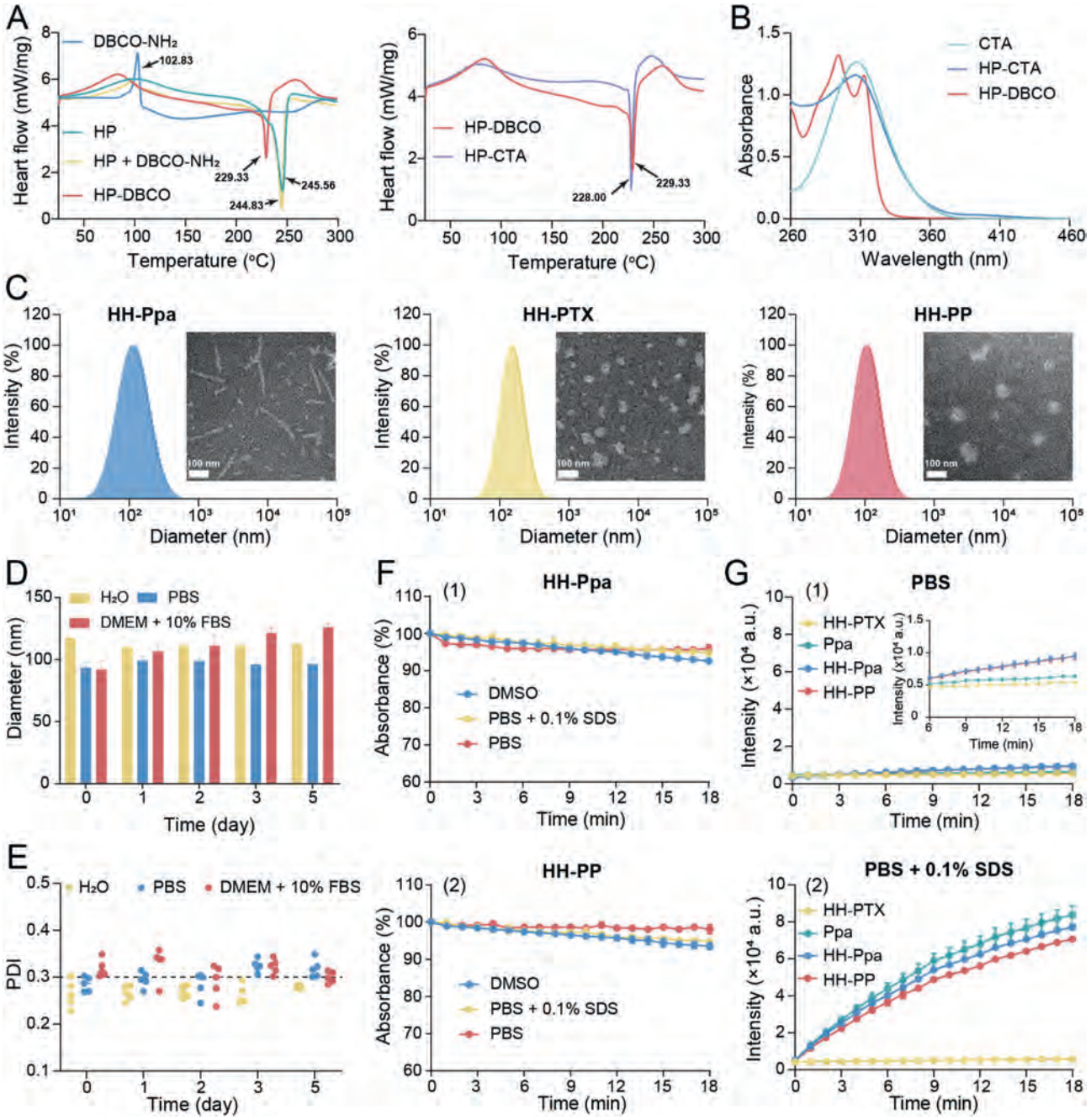

Figure 1 Schematic illustration of preparation and characterizations of HH-Ppa, HH-PTX, and HH-PP. (A) DSC curves of HP, DBCO-NH_2, HP-DBCO, a mixture of HP and DBCO-NH_2, and HP-CTA. (B) UV absorbance spectra of CTA, HP-DBCO, and HP-CTA. (C) The hydrodynamic size distributions and TEM images of HH-Ppa, HH-PTX, and HH-PP (scale bar = 100 nm). (D) The colloidal stability and (E) PDI variations of HH-PP in H_2O, PBS, and DMEM (with 10% FBS) for 5 days (n = 5). (F) Photostability of HH-Ppa (1) and HH-PP (2) in DMSO, PBS, and PBS with 0.1% SDS after irradiation (n = 3). (G) Variations in the SOSG fluorescence intensity *versus* the irradiation time after incubation with Ppa, HH-Ppa, and HH-PP in PBS (1) or PBS with 0.1% SDS (2) under irradiation, HH-PTX as a control (n = 3). Data are presented as mean ± SD.

the diameter of the co-assembled HH-PP decreased to 106.4 ± 1.6 nm (Table S5). The zeta potentials of HH-Ppa, HH-PTX, and HH-PP were −14.0 ± 1.0, −24.6 ± 1.7, and −19.5 ± 1.3 mV, respectively, indicating that three polymers could circulate in the blood without engulfment by the reticuloendothelial system (Supporting Information Table S6). Notably, the resulting HH-PP exhibited a uniform spherical morphology as confirmed by transmission electron microscopy (TEM), which was different from the nanofiber morphology of HH-Ppa and an irregular shape of HH-PTX (Fig. 1C). These results indicate that HH-PP was not a physical mixture, but a co-assembled product. This stable co-assembly configuration was essential for effectively co-delivery of Ppa and PTX and their synergistic action within tumor cells.

This co-assembly technology could not only coordinate the action of the two drugs in tumor cells but also improve their stability under storage conditions and in a physiological

environment. The stability results demonstrated that HH-PP exhibited high stability with negligible alterations in the particle size or PDI in H_2O, PBS, and DMEM with 10% FBS over 120 h, thereby supporting prolonged circulation and preventing premature release (Fig. 1D and E, Supporting Information Fig. S18). In addition, photostability analysis confirmed that co-assembly improved the photostability of the photosensitizer in different solutions. HH-PP exhibited a 5.3% loss in the absorbance in PBS with 0.1% SDS and a 7.4% loss in DMSO, indicating a slower degradation rate compared to HH-Ppa alone (Fig. 1F). Furthermore, we evaluated the ability of HH-Ppa to generate singlet oxygen, a critical ROS for the induction of ferroptosis[38], using a singlet oxygen sensor green (SOSG) reagent. The results showed that HH-Ppa and HH-PP produced a significantly elevated level of singlet oxygen under laser irradiation compared with Ppa when dissolved in PBS (Fig. 1G (1)). Additionally, the fluorescence intensity of SOSG was significantly enhanced when the assembly structures of HH-Ppa and HH-PP were disrupted in the presence of SDS. (Fig. 1G (2)). Overall, these findings demonstrated that our rationally designed HH-PP was a stable co-assembly nanomedicine for co-delivering Ppa and PTX, which could facilitate their tumor accumulation and enhance their synergistic effects on amplifying ferroptosis and the overall anti-tumor efficacy.

3.2. *In vivo penetration and in vitro infiltration*

The metabolic clearance in the circulation system was evaluated by pharmacokinetic analysis of HH-Ppa, ^{Rox}HH-PTX, ^{Rox}HH-PP, free Ppa, and free Rox. ^{Rox}HH-PP prolonged the circulation time of HH-Ppa and free Ppa. The half-life time ($t_{1/2}$) of Ppa in ^{Rox}HH-PP was 15.6- and 24.9-fold longer than that in HH-Ppa and free Ppa, respectively. The area under the curve (AUC) of ^{Rox}HH-PP was 1.8- and 6.8-fold larger than that of HH-Ppa and free Ppa. ^{Rox}HH-PP slightly prolonged the circulation time of ^{Rox}HH-PTX. The $t_{1/2}$ was 72.34 h in ^{Rox}HH-PP and 59.17 h in ^{Rox}HH-PTX. The AUC of ^{Rox}HH-PP was 1.4-fold larger than that of ^{Rox}HH-PTX (Fig. 2A and B, Supporting Information Tables S7 and S8). Next, the *in vivo* distribution of HH-Ppa, ^{Rox}HH-PTX, ^{Rox}HH-PP was observed with living imaging. HH-Ppa, ^{Rox}HH-PTX, and ^{Rox}HH-PP were injected into 4T1 tumor-bearing nude mice through tails, and Rox and Ppa signals were monitored at different pre-set time points (Supporting Information Fig. S19). Compared to ^{Rox}HH-PTX and HH-Ppa, ^{Rox}HH-PP displayed stronger fluorescence signals of Rox and Ppa *in vivo* at all time points (Fig. 2C and Supporting Information Fig. S20A). In contrast to the faint fluorescence signal observed in the free Ppa group at 24 h post-injection, HH-Ppa and ^{Rox}HH-PP displayed strong fluorescence signals at 72 h post-injection (Fig. S20A). Both pharmacokinetic analysis and live imaging results suggested ^{Rox}HH-PP had a prolonged circulation duration compared to HH-Ppa, ^{Rox}HH-PTX, and free Ppa.

The mice tumors and organs were collected at the end of the living imaging experiment and followed with *ex vivo* fluorescence imaging to investigate the distribution of nanoparticles. Stronger fluorescence signals in tumors after treatment with ^{Rox}HH-PP compared to those treated with ^{Rox}HH-PTX and HH-Ppa (Fig. 2D and E, Fig. S20B and S20C). Frozen sections of tumors were analyzed to analyze the tumor penetration ability of ^{Rox}HH-PTX, HH-Ppa, and ^{Rox}HH-PP. Results showed that both Ppa and Rox signals could be detected in both the peripheries and central zones of the tumors after treatment with ^{Rox}HH-PP, which confirmed that ^{Rox}HH-PP could penetrate deeply into the tumor tissue after it was intravenously injected into these mice (Fig. 2F).

The PTX concentration in the blood and the tumor tissue before laser irradiation and at different time points post-irradiation after a single injection of HH-PP was quantified by LC−MS/MS to assess the targeted release of PTX from HH-PP in the tumor tissue. The results showed that free PTX in the serum exhibited a very low concentration, which was below five nanograms (ng) per 200 μL serum. By contrast, the PTX concentration in the tumor tissue was much higher than that in the serum. The PTX concentration was 63.02 ± 16.49 ng per 100 mg tumor tissue, and it increased to 110.52 ± 20.22 ng per 100 mg tumor tissue after laser irradiation. The PTX concentration in the tumor tissue was gradually decreased to the level before laser treatment at 24 h post-irradiation. These results illustrate that HH-PP could be stable in the circulation system. PTX could be released in tumor tissues, and laser irradiation efficiently promoted its release from HH-PP in the tumor tissue (Supporting Information Fig. S21).

To further assess the penetration ability of ^{Rox}HH-PP in cancer cells, multicellular spheroids (MCSs) from 4T1 cells were prepared and precultured with ^{Rox}HH-PP before CLSM analysis. These results shown in Supporting Information Fig. S22 confirmed there were strong fluorescence signals of Ppa and Rox from the periphery to the inner zone of MCSs, which further supported deep penetration of HH-PP within tumor tissues. Additionally, we evaluated the cellular uptake of ^{Rox}HH-PP by 4T1 cells and its intracellular distribution in organelles. 4T1 cells were co-cultured with ^{Rox}HH-PP, and the fluorescence signals of Rox in ^{Rox}HH-PTX and ^{Rox}HH-PP, as well as Ppa in HH-Ppa and ^{Rox}HH-PP, were captured using CLSM at different time points. The results in Supporting Information Fig. S23A showed that fluorescence signals of Ppa and Rox could be detectable at hour 2, and their signal intensity was gradually enhanced as the incubation time extended. The fluorescence signals were semi-quantified *via* flow cytometry after internalization by 4T1 cells to compare the cellular uptake levels of different nanoformulations. Both CLSM images and flow cytometry results suggested the fluorescence signal of either Ppa or Rox was statistically intensified in 4T1 cells co-cultured with ^{Rox}HH-PP compared to those without any treatment. However, there was no statistical difference in the Ppa signal intensity in the cells after uptake of HH-Ppa and ^{Rox}HH-PP, nor the Rox signal intensity in the cells after uptake of ^{Rox}HH-PTX and ^{Rox}HH-PP (Fig. 2G and H, Fig. S23B), suggesting co-assembled formulation, ^{Rox}HH-PP, could be internalized by 4T1 cells at a similar level as ^{Rox}HH-PTX and HH-Ppa. Intracellular distribution of ^{Rox}HH-PP in organelles was further revealed. Colocalization of the signal from organelle trackers and the signals of Rox and Ppa in ^{Rox}HH-PP was captured using CLSM. The CLSM images supported that there was a wide intracellular distribution of ^{Rox}HH-PP after its internalization, and it was seen in organelles, including mitochondria, lysosomes, and the endoplasmic reticulum (ER) (Fig. 2I and J, Supporting Information Figs. S24−S26). All these results suggested that ^{Rox}HH-PP had a remarkable extension in its circulation time, a pronounced penetration ability in tumor tissues, a high level of cellular uptake, and a wide distribution in organelles after internalization, and these attributes of ^{Rox}HH-PP may fundamentally contribute to its potent anti-tumor effects.

3.3. *In vitro anticancer potency*

To assess the synergistic effects of HH-PP, the anti-tumor efficacy of HH-PP against 4T1 cells was investigated. First, the cytotoxicity of HH-PP at different ratios of HH-PTX to HH-Ppa was

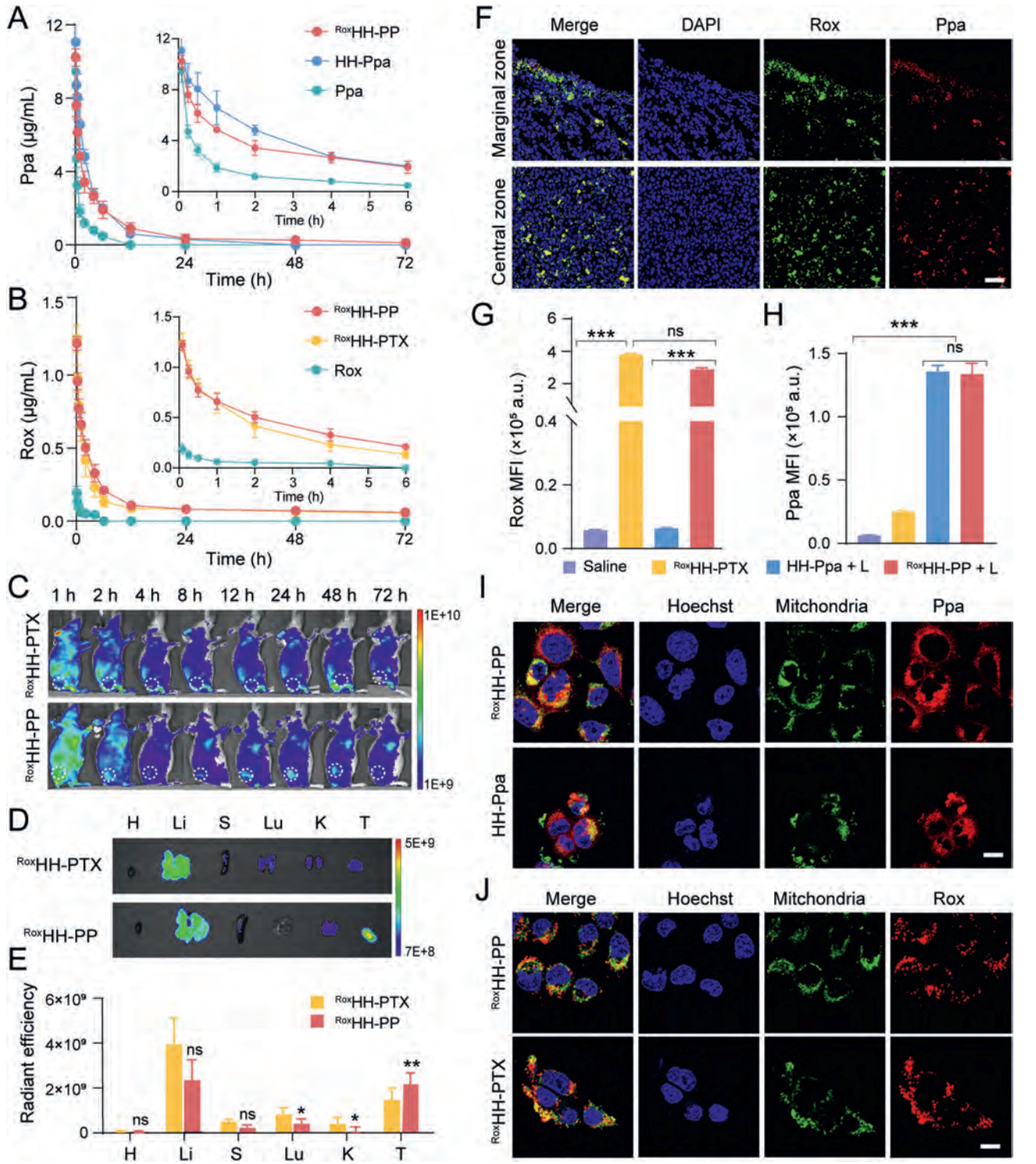

Figure 2 *In vivo* distribution and *in vitro* infiltration. (A) and (B) Pharmacokinetic analysis of HH-Ppa, ^{Rox}HH-PTX, or ^{Rox}HH-PP ($n = 4$). (C) Fluorescent living image for Rox signals in tumor-bearing nude mice after treatment with ^{Rox}HH-PTX or ^{Rox}HH-PP. White circles for tumors. (D) *Ex vivo* fluorescent images for Rox signals in the main organs and tumors at 72 h post-injection (H: heart, Li: liver, S: spleen, Lu: lung, K: kidney, T: tumor). (E) Semi-quantitative radiant efficiency of Rox from (D) ($n = 4$). ^{Rox}HH-PP group was compared with ^{Rox}HH-PTX group. (F) Fluorescent images of frozen tumor sections from (D) (scale bar = 50 μm). (G) and (H) MFI of Rox and Ppa signals in the cells after uptake of HH-Ppa, ^{Rox}HH-PTX, or ^{Rox}HH-PP *via* flow cytometry ($n = 3$), respectively. (I) and (J) Representative CLSM images for co-localization of signals for organelles and Rox or Ppa signals (scale bar = 20 μm). Data are presented as mean ± SD. ns, not significant. $^*P < 0.05$. $^{**}P < 0.01$. $^{***}P < 0.001$.

evaluated using CCK-8 assays to calculate the combination index (CI) *via* the CompuSyn software. The optimal synergism of HH-PP under irradiation was observed at a mass ratio of HH-PTX to HH-Ppa of 1:1, displaying the lowest CI in the fraction affected (Fa) range of 0.15−0.85 (Supporting Information Fig. S27). This was in accordance with the results of particle size and PDI of HH-PP (Fig. S17, Table S5). Therefore, HH-PP with a mass ratio of HH-PTX to HH-Ppa of 1:1 was used for the following studies. Cell death staining was applied for cytotoxicity of the nanoformulations against 4T1 cells. A higher percentage of dead cells indicated by positive PI staining appeared in the HH-PP and laser irradiation treated group (HH-PP + L) compared to HH-PTX and HH-Ppa + L group (Fig. 3A). A commonly used method to assess cytotoxicity *via* an apoptosis kit was then applied. There were no positively stained cells in the early apoptosis quadrant after incubation with HH-PP (Supporting Information Fig. S28). These treated cells were aggregated, which may be due to disturbed cell membranes after treatment with HH-PP + L, and apoptotic cells were barely detected in flow cytometry plots. The results suggest that 4T1 cell death after the treatment of HH-PP + L may not be due to apoptosis.

To unveil the predominant inducing mechanism for synergistic cytotoxicity exerted by HH-PP + L, the anti-tumor efficacy of Ppa and PTX against 4T1 cells was assessed separately. Morphological changes in cellular microtubules and microfilaments after 24-h treatment with HH-PTX or HH-PP were observed. The images revealed a similar level of shrinkage in the HH-PTX and HH-PP groups. The uniform distribution of tubulin and actin in the plasma was seen in the control group (Fig. 3B and Supporting Information Fig. S29). Cytotoxicity of Ppa has been ascribed to

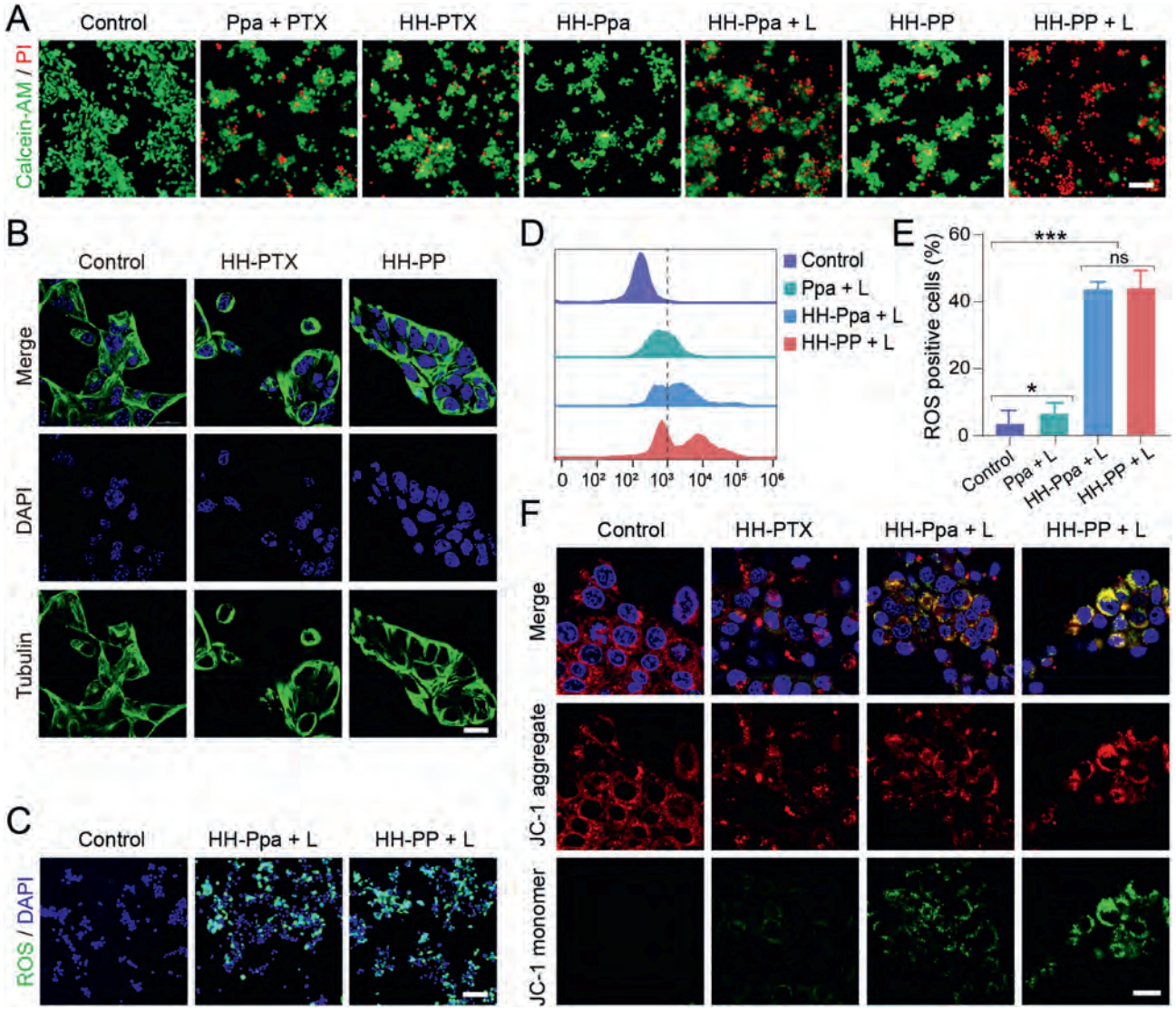

Figure 3 *In vitro* anticancer treatment with HH-PP and irradiation. (A) Cell death staining after treatment with different formulations (scale bar = 100 μm). (B) 4T1 cell microtubule aggregation after treatment with HH-PTX and HH-PP for 24 h (scale bar = 20 μm). (C) ROS staining images and (D) flow cytometry results of the cells treated with HH-Ppa and HH-PP under irradiation (scale bar = 100 μm). (E) Statistical histogram of (D) ($n = 3$). (F) Representative CLSM images for the mitochondria membrane potential stained with JC-1 in the cells treated with HH-PTX, HH-Ppa, and HH-PP under irradiation (scale bar = 20 μm). Data are presented as mean ± SD. ns, not significant. $^{*}P < 0.05$. $^{***}P < 0.001$.

ROS generation under irradiation. Therefore, ROS generation was evaluated in the cells after treatment with Ppa-containing nanoformulations. Fluorescence images revealed that there were abundant cells with positive ROS signals after treatment with either HH-Ppa or HH-PP under irradiation (Fig. 3C), and flow cytometry analysis confirmed similar levels of intracellular ROS production in the cells treated with HH-Ppa and laser irradiation (HH-Ppa + L) and HH-PP + L (Fig. 3D and E). These results indicated that neither PTX nor Ppa played a dominant role in synergistic cytotoxicity in HH-PP.

Since HH-PP was distributed in different cellular organelles after internalization, the effects of HH-PP on several organelles were evaluated to demystify the mechanism(s) for synergistic cytotoxicity of HH-PP in addition to the therapeutic action of Ppa and PTX. The mitochondrial function was evaluated with a mitochondrial membrane potential kit, JC-1. JC-1 aggregates appeared in the cells without any treatment in the control group, suggesting a high mitochondrial potential in the normal mitochondria. In contrast, after culturing with different formulations for 12 h, a stronger signal of JC-1 monomers appeared in the HH-PP + L-treated group, suggesting a low mitochondria potential in the abnormal mitochondria (Fig. 3F, Supporting Information Fig. S30). An apoptosis morphology with condensation of the cytoplasm represented by a darker color of the cytoplasm and shrinkage of cells represented by a smaller diameter were observed in the TEM image of the 4T1 cells treated with HH-PTX. By contrast, 4T1 cells treated with HH-Ppa + L and HH-PP + L revealed apparently different morphologies. Furthermore, cells in the HH-PP + L-treated group with an enhancement in the ER membrane gap, suggesting these cells experienced much more severe ER stress compared to the cells in the treatment group of HH-Ppa + L (Supporting Information Fig. S31). These results implied that co-assembled HH-PP not only induced microtube and microfilament inhibition from HH-PTX and ROS generation from HH-Ppa under irradiation but also influenced the ER and mitochondrial function. All these factors could contribute to synergistic cytotoxicity of HH-PP, triggering a different cell death type instead of apoptosis.

3.4. Inducing of ferroptosis in tumor cells by HH-PP

HH-PP + L-treated cells revealed an abnormal morphology of mitochondria with an increase in the mitochondrial membrane density indicated by a darker color of the mitochondrial inner membrane and a reduction in the mitochondrial cristae indicated by a widened space between the mitochondrial cristae, suggesting the predominant cell death mode in these tumor cells may be ferroptosis (Fig. 4A). Severe swelling with bubbles on the plasma membranes in these cells after treatment was observed in the HH-PP + L group (Fig. 4B). Although the cytoplasmic feature of cell swelling is a typical morphology of pyroptosis, our next study on pyroptosis-associated protein expression did not support the cell death mode of pyroptosis. Specifically, we investigated the expression levels of key proteins associated with pyroptosis in 4T1 cells, including the N-terminal fragment of Gasdermin-D (GSDMD-N) and its upstream protein cleaved caspase-1[2,39,40]. There were no statistical differences in the expression levels of GSDMD-N and cleaved caspase-1 in tumors among these treatment groups, implying pyroptosis may not be sufficiently induced in the HH-PP + L treatment group compared to other groups. No statistical difference in the expression level of cleaved caspase-3 was seen in tumor tissues between the treatment by HH-PTX and HH-PP + L, implying no enhanced apoptosis in the HH-PP + L treatment group compared to other groups (Supporting Information Fig. S32). Since the swelling appearance that was an indicator of damaged cell membranes could be observed in ferroptosis[41], the abnormal morphology of the cells treated with HH-PP + L, specifically, their shape and size and their mitochondrial texture, suggested the principal cell death mode in these tumor cells may be ferroptosis.

Ferroptosis is a regulated cell death characterized by overwhelming intracellular lipid oxidation[42]. The most common trigger of lipid oxidation is GSH depletion accompanied by a decrease in the GPX4 expression or deactivation of GPX4[43]. Therefore, the GPX4 expression and the GSH content were investigated to confirm ferroptosis triggered by HH-PP + L treatment. The expression of GPX4 in the tumor tissue was evaluated after mice were treated with formulations for 24 h and irradiated for another 24 h. Immunohistochemistry images of GPX4 revealed that the mice tumors treated with HH-PP + L had a lower expression of GPX4 than those in other treatment groups (Fig. 4C). The content of the intracellular antioxidant substance, GSH, was decreased after treatment with HH-PP + L compared to the control and other treatment groups (Fig. 4D). These effects induced by HH-PP + L could directly trigger lipid oxidation.

The lipid oxidation degree was then investigated. MDA, the lipid oxidation end product, was detected to confirm the level of oxidative lipids in the HH-PP + L-treated cells (Fig. 4E and Supporting Information Fig. S33). An oxidized lipid tracker, BODIPY 581/591 C11, was employed to reveal the level of lipid peroxidation (LPO) in cells. Representative CLSM images showed that the proportion of cells with LPO was remarkably increased in the HH-PP + L group compared to other treatment groups or the control group (Fig. 4F). It was also revealed that oxidation state of BODIPY 581/591 C11 staining was dispersed in the entire cytoplasm other than on the cell membrane only, suggesting a wide impact on the intracellular lipids triggered by HH-PP + L treatment (Fig. 4F). Flow cytometry analysis revealed the proportion of cells with positive LPO staining increased to 89.98% in the HH-PP + L-treated group, compared to 0.13% in the control group (Fig. 4G and Supporting Information Fig. S34). After cells experienced ferroptosis, the overwhelming intracellular lipid oxidation could eventually interrupt cell membranes (Fig. 4B). A much higher level of LDH was released from cells after exposure to HH-PP + L compared to that in the control group, suggesting the cell membrane may be damaged in the cells with HH-PP + L treatment (Fig. 4H). These results confirmed that cells treated with HH-PP + L experienced reinforced ferroptosis, evidenced by typical morphological and biochemical characteristics.

3.5. Ferroptosis caused by lipid disorder

Lipid oxidation is a key process in ferroptosis, and it is highly dependent on lipid compositions[44]. To reveal the impact of the treatment with HH-PP + L on lipid compositions in 4T1 cells, non-targeted lipidomics analysis was employed to evaluate the levels of intracellular lipid oxidation and lipid modulation. After 4T1 cells were treated with HH-PP + L, intracellular lipid was extracted, the lipid samples were run on LC−MS/MS, and lipids were identified *via* MS-DIAL. A total of 1892 lipids in different lipid categories were extracted and identified. Principal component analysis (PCA), a commonly used data analytics method for classification in lipidomic datasets, was applied and confirmed the differences between the cells treated with HH-PP + L and the control cells *via* the SIMCA 16.0 software (Fig. 5A). The changes

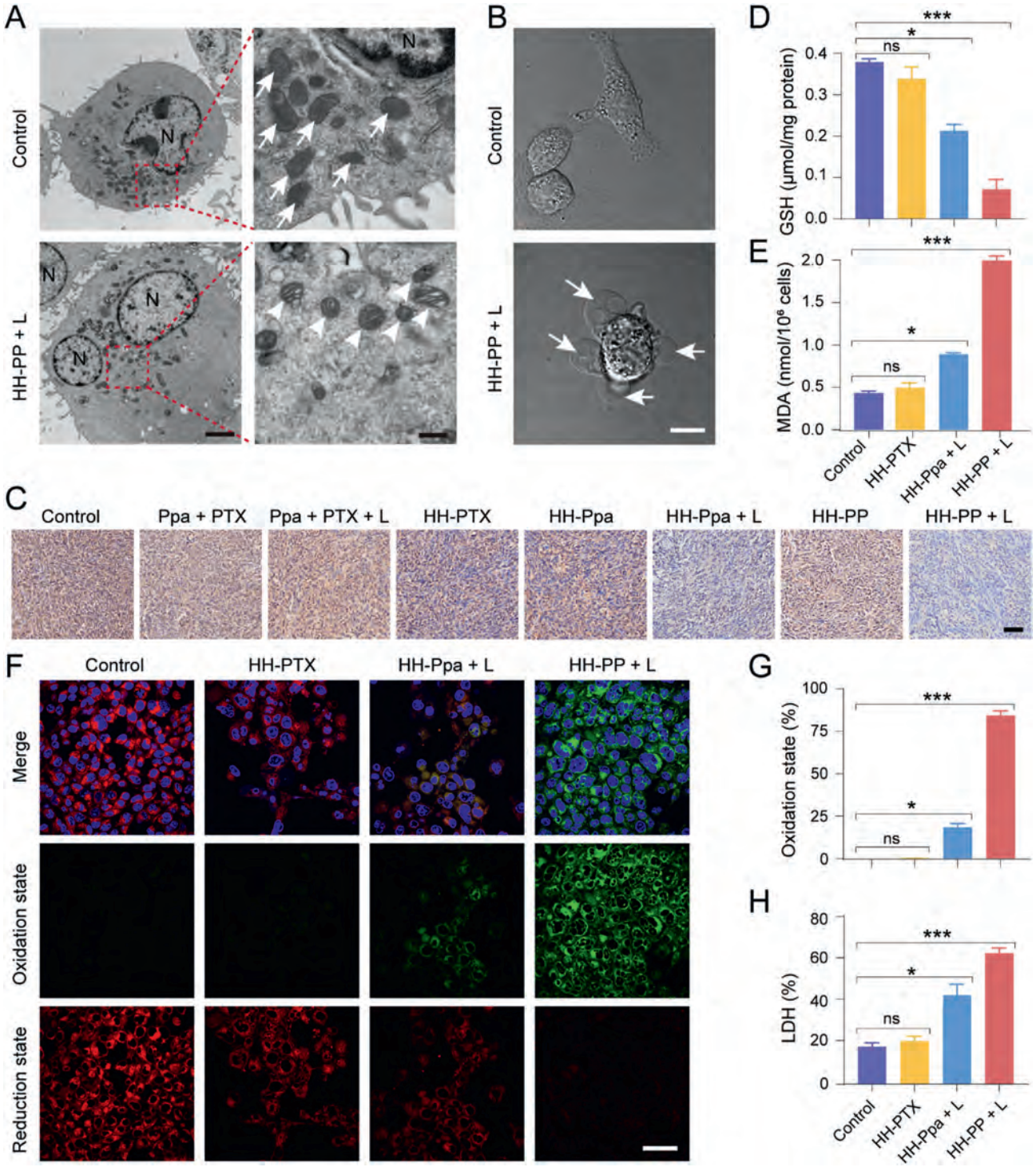

Figure 4 Characteristics of ferroptosis of 4T1 cells by HH-PP + L. (A) TEM images of mitochondria with characteristic morphologies due to ferroptosis. Arrows point to a normal morphology of mitochondria in the control group, and arrowheads point to an abnormal morphology with an increase in the mitochondrial membrane density in the cells treated with HH-PP + L. (scale bar = 2 μm for a low-power microscope (left); 0.2 μm for a high-power microscope (right)). (B) Bright field microscope images for swelling of the cells treated with HH-PP + L (scale bar = 10 μm). (C) Immunofluorescence staining images of GPX4 in tumors on Day 1 after treatment with different nanoformulations (scale bar = 100 μm). (D) Quantitative intracellular GSH levels and (E) MDA release after the cells were treated with HH-PTX, HH-Ppa + L, and HH-PP + L ($n = 3$). (F) Representative CLSM images for lipid oxidation (scale bar = 10 μm), and (G) Oxidative lipids quantified by flow cytometry ($n = 3$). (H) Levels of LDH release after the cells were treated with HH-PTX, HH-Ppa + L, and HH-PP + L ($n = 3$). Data are presented as mean ± SD. ns, not significant. $^*P < 0.05$. $^{***}P < 0.001$.

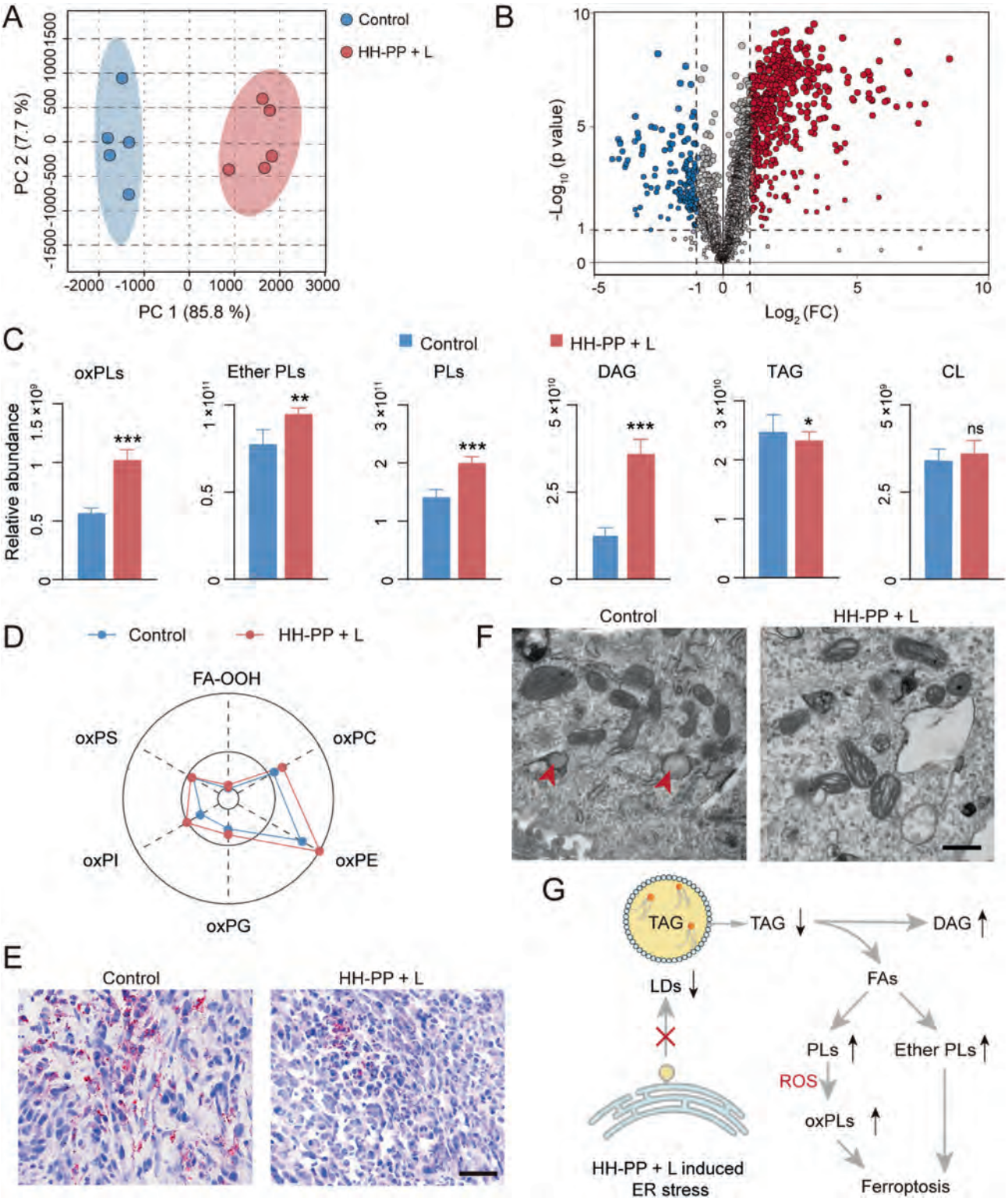

Figure 5 Ferroptosis-associated lipid metabolism disorder. (A) PCA analysis of lipid samples from the control cells and the cells treated with HH-PP + L. (B) Volcano plot to distinguish the difference in lipids between the control cells and the HH-PP + L-treated cells. The X-axis was the fold change (FC) in the relative abundance of lipid species, and the Y-axis was the *P* value. (C) Relative abundance of lipids species in different categories ($n = 5$). (D) Radar image for the proportions of oxidative lipids in different categories. (E) Oil Red O staining of tumor frozen sections (scale bar = 50 μm). (F) Representative TEM image for cellular LDs. They were broken down in the HH-PP + L-treated group. Arrowheads point to LDs in control cells (scale bar: = 0.2 μm). (G) Schematic diagram of lipid metabolism disorder after treatment with HH-PP + L. Data are presented as mean ± SD. ns, not significant. $^{*}P < 0.05$. $^{**}P < 0.01$. $^{***}P < 0.001$.

in individual lipids were evaluated *via* a heat map. Ubiquitous variations throughout all categories of lipids were seen between HH-PP + L-treated cells and the control cells (Supporting Information Fig. S35). Specifically, 533 lipids were statistically upregulated, and 154 lipids were downregulated in the cells treated with HH-PP + L (Fig. 5B). Lipids abundance in each category was analyzed to display the degree of lipids variations in different categories, and oxidative lipids were statistically increased in the HH-PP + L-treated cells (Fig. 5C). To distinguish oxidative lipid variations, a radar plot was applied to present variations in individual types of oxidative lipids. The results showed that the most abundant species in the oxidative lipid type was oxPE, which is a main component of cell membranes. Other oxidized lipids species, including oxidized free fatty acids (FAs), oxidized phosphatidycholine (oxPC), oxPE, oxidized phosphatidylglycerol (oxPG), oxidized phosphatidylinositol (oxPI), and oxidized phosphatidylserine (oxPS), were also increased in the cells with HH-PP + L treatment compared to the cells without any treatment (Fig. 5D). Among these 111 oxidative lipids detected by LC−MS/MS, 40 of them were statistically increased in the HH-PP + L-treated cells compared to the control, and 33 of them were increased with a Log_2 (FC) of greater than 1 (Supporting Information Fig. S36). Therefore, HH-PP treatment of tumor cells with irradiation resulted in the oxidation of a wide spectrum of lipids in various categories, suggesting that the oxidizing reaction of these intracellular lipids did not have an apparent preference for lipid categories and structures.

Apart from increased oxidative lipids, ubiquitous lipid disorder without structure diversity throughout all categories of lipids (Supporting Information Fig. S37) implied lipid synthesis, metabolism, transformation, and storage may be modulated after treatment with HH-PP + L. To unveil the mechanism for the modulation of the lipids in the tumor cells, we evaluated statistically significant lipid variations in different categories in the cells between the HH-PP + L group and the control group by estimating the relative abundance of lipids in different categories, especially triacylglycerol (TAG) and diacylglycerol (DAG). In cells, there is a dynamic equilibrium between these two related lipids and phospholipids (PLs). Specifically, FAs, as a substitute group of TAGs, DAGs, and PLs, could be shuttled among these lipids[45]. There are three FAs in the structure of TAGs, which could release one FA to generate DAGs, and they could be easily packaged for PLs synthesis. Excess PLs inside the cells could be oxidized by ROS to form oxPLs (including oxPC, oxPE, oxPG, oxPI, and oxPS). Either ether PLs and oxPLs could eventually trigger ferroptosis. On the contrary, the storage of FAs in TAGs could reduce the FAs pool and inhibit PLs formation, which could lead to a reduction in membrane lipids oxidation. It is noted that there was a remarkable increase in DAGs and PLs, but a decrease in TAGs, implying HH-PP + L triggered ferroptosis in cells through decreasing TAGs and increasing PLs (Fig. 5C).

TAGs and other categories of neutral lipids, such as CLs, are stored in lipid droplet (LD) to serve as a source for antioxidation[46]. We then accessed LD content in the cells after treatment with HH-PP + L to evaluate TAG storage. LDs could be observed in the control cells in the Oil Red O staining images and TEM images. They were barely seen in the cells after treatment with HH-PP + L, suggesting the TAG storage vesicles were reduced by the intervention of HH-PP + L (Fig. 5E and F). Furthermore, the cells treated with HH-PP + L experienced ER stress may also inhibit lipid synthesis, resulting in decreased TAG content and LD breakdown (Fig. S31). Therefore, intervention with HH-PP + L could increase lipid oxidation through LD breakdown and TAG degradation, eventually inducing ferroptosis (Fig. 5G, Supporting Information Fig. S38).

3.6. ICD induced by ferroptosis

During ferroptosis, the adaptive immune response system, which plays a dominant role in immune surveillance and immune attack of tumor cells to suppress tumor progression, could be activated[47]. To be specific, tumor cell membranes are disrupted by lipid oxidation to release DAMPs. HMGB1 released from cell nuclei and CRT exposed to cell membranes are the most significant DAMPs, which can induce DCs maturation and promote immune cell proliferation. The adaptive immunoreaction response could eventually suppress tumor proliferation[48]. We first studied released DAMPs, including HMGB1 and CRT, to assess adaptive immunoreaction activation. HMGB1 is primarily located in the nucleus, and it acts as a companion for DNA in a normal situation. It can also be shuttled to the cytoplasm as a typical DAMP. CRT is a major calcium-binding protein, and it is normally located in the ER. It can be overexpressed and secreted to cell membranes to enhance cell immunogenicity. As shown in Fig. 6A, the level of HMGB1 in the nucleus decreased after treatment with HH-PP + L, resulting in its translocation to the cytoplasm and subsequent release into the extracellular space. CRT was uniformly distributed in the cytoplasm, and it was also exposed to the cell membrane surface in the treatment group with HH-PP + L. The signal of CRT was the strongest in the HH-PP + L-treated group. Therefore, ferroptosis induced ICD in tumor cells to release DAMPs, which sent an "eat me" signal to the immune surveillance system for antigen presentation.

Activation of DCs maturation after the stimulation of tumor cells treated with HH-PP + L was assessed *in vitro*. Fig. 6B illustrates the protocol for the cultivation and activation of BMDCs. In brief, bone marrow cells were harvested, and their differentiation into BMDCs was stimulated. Meanwhile, 4T1 cells were co-cultured with HH-PTX, HH-Ppa, and HH-PP for 24 h and another 12 h after irradiation. The spent media from 4T1 cells were added into the cell culture media of BMDCs for 24 h cultivation. The level of DCs maturation was analyzed *via* flow cytometry by evaluating the portion of matured DCs, which were cells with $CD80^+CD86^+$ in $CD11c^+$ DCs. The portion of mature DCs was 17.85% in BMDCs in the control group. In comparison, it was increased to 38.65% in BMDCs co-cultured with the spent media after 4T1 cells were treated with HH-PP + L, and this was statistically higher than that in BMDCs that were co-incubated with the spent media after treatment of tumor cells with HH-PTX and HH-Ppa + L (Fig. 6C and D). Therefore, HH-PP + L treatment of tumor cells could activate DCs maturation and induce adaptive anti-tumor immunity responses.

DAMPs release and immune cell proliferation were also studied *in vivo*. Mice were intravenously injected with different formulations through tail veins, and the tumor tissues in PTX + Ppa + L, HH-Ppa + L, and HH-PP + L treatment groups were exposed to laser for irradiation at 24 h post-injection. DAMPs expression levels and immune cell densities in tumor tissues were detected *via* immunofluorescence staining at 48 h post-injection. The levels of HMGB1 and CRT were elevated in the HH-PP + L-treated group compared to those in other groups (Fig. 6E−G). T cells, the major type of immune cells related to adaptive immune responses, were investigated. Among these T cells, $CD8^+$ cytotoxic T cells (CTLs) have been considered as the

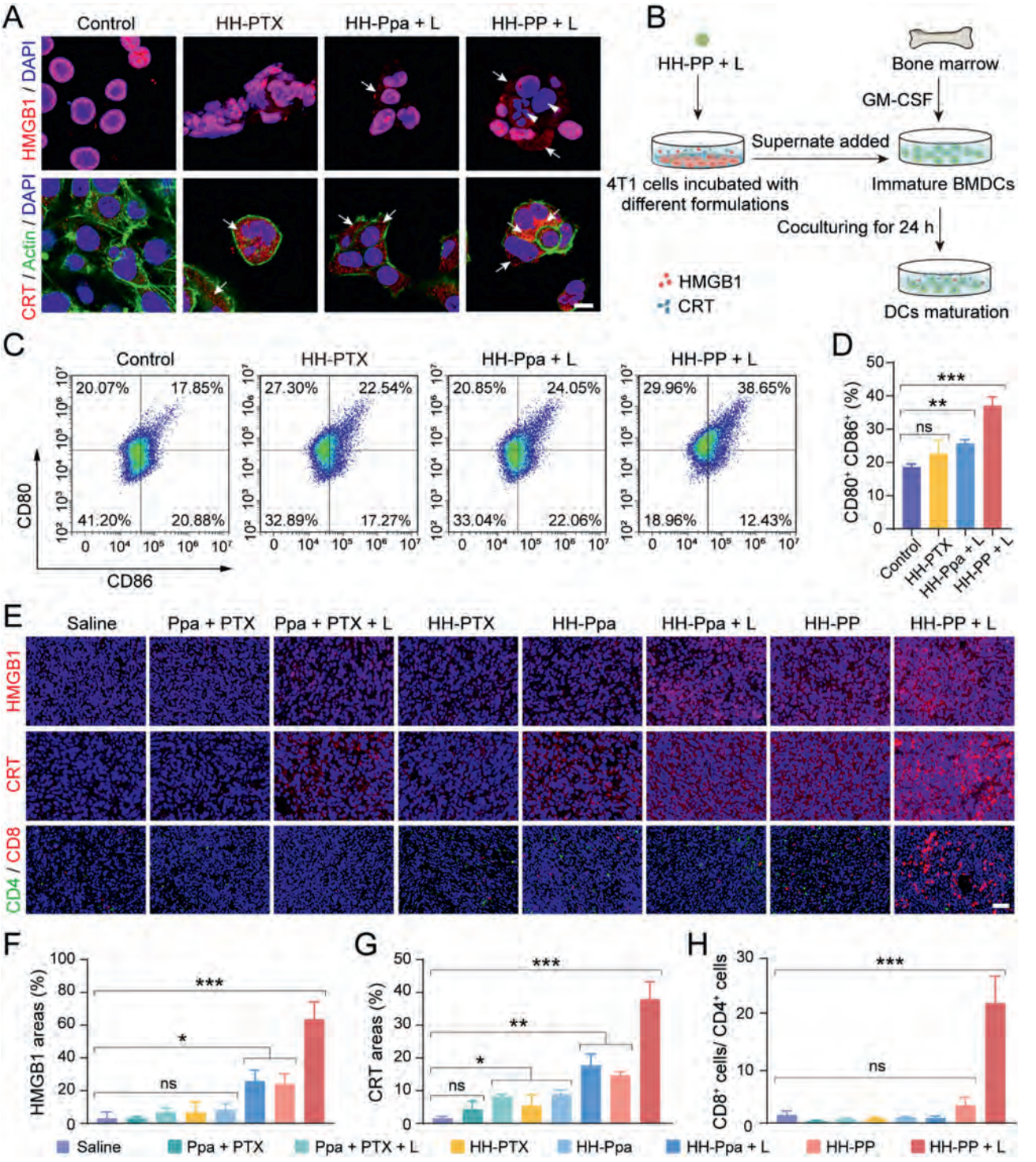

Figure 6 ICD effects and activation of DC maturation. (A) Representative CLSM images for HMGB1 releasing from the cell nuclear and CRT exposure on the cell surface in 4T1 cells after coculturing with HH-Ppa and HH-PP for 12 h, irradiation for 30 s, and incubation for another 6 h. Cells in HH-PTX were cultured for 18 h (scale bar = 10 μm). (B) Schematic procedure for bone marrow dendritic cells (BMDCs) collection, cultivation, and maturation. (C) Flow cytometry plots and (D) quantitative results of matured BMDCs by analyzing the proportion of $CD80^+CD86^+$ cells in $CD11c^+$ DCs ($n = 3$). (E) Representative immunofluorescence staining images of HMGB1, CRT, CD4, and CD8 in tumor tissues on Day 1 after treatment with nanoformulations (scale bar = 20 μm). Statistical histogram of levels of HMGB1 (F), CRT (G), and ratios of $CD8^+$ T cells to $CD4^+$ T cells (H) extracted from (E) ($n = 5$). Data are presented as mean ± SD. ns, not significant. $^*P < 0.05$. $^{**}P < 0.01$. $^{***}P < 0.001$.

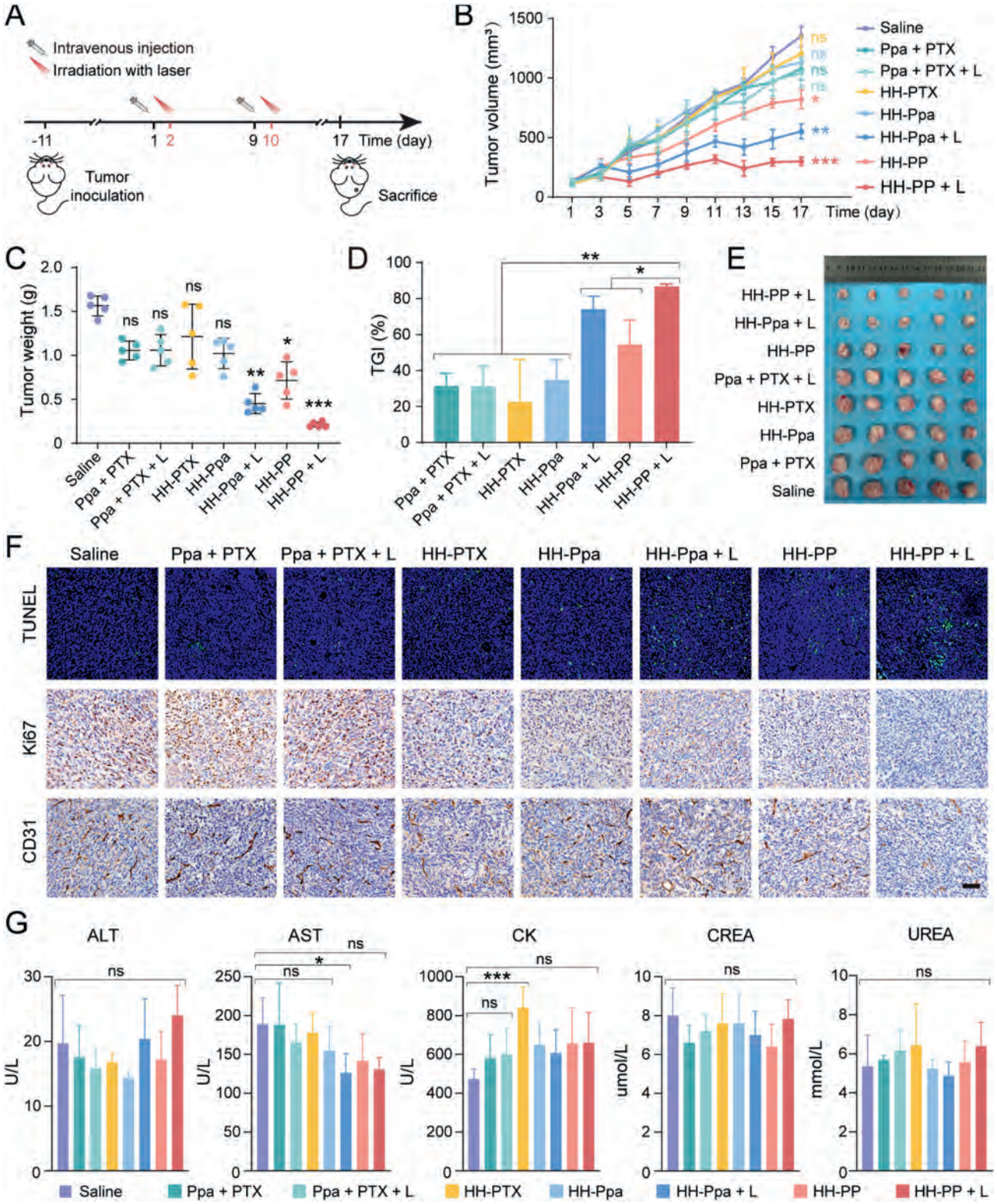

Figure 7 *In vivo* anticancer efficacy study. (A) Experimental flow chart. The mice in the PTX + Ppa + L, HH-Ppa + L, and HH-PP + L groups received irradiation at 24 h post-injection of these formulations. (B) The average tumor volume in each treatment group during the experimental period of 17 days ($n = 5$). (C) The average tumor weight in different treatment groups at the end of the experiment ($n = 5$). (D) Tumor growth inhibitions (TGIs) were calculated from the tumor weight in (C). (E) Photos of dissected tumors. (F) Immunofluorescence and immunohistochemistry staining images of tumors from (E), scale bar = 50 μm. (G) Blood biochemistry indicators for the function of the liver, heart, and kidney ($n = 4$). Data are presented as mean ± SD. ns, not significant. *$P < 0.05$. **$P < 0.01$. ***$P < 0.001$.

anti-tumor immune effector cells for attacking tumor cells. CTLs can produce perforin, granzymes, and cytokines to induce tumor cell death but keep nonmalignant cells intact. $CD4^+$ T helper (Th) cells are reported to provide cytokine-mediated support for CTLs expansion and their function. It was observed that CTLs proliferated, and their infiltration level was increased in the tumor tissues in the HH-PP + L treatment group compared to the other groups. There were no significant differences in the Th cells number among all experimental groups (Fig. 6E). Thus, the ratio of $CD8^+$ T cells to $CD4^+$ T cells was remarkably boosted in the HH-PP + L-treated group compared to other treatment groups (Fig. 6H). Therefore, the anti-tumor efficacy of HH-PP was strengthened through enhancing immunogenic responses, supported by DAMPs release, DCs maturation, and CTLs proliferation, eventually suppressing tumor progression.

3.7. In vivo anticancer effects of HH-PP

To evaluate the *in vivo* anti-tumor effect of HH-PP, tumor-bearing mice were grouped and intravenously injected with different nanoformulations (Fig. 7A). There were two injections on Days 1 and 9, and irradiation was implemented on Days 2 and 10 in the groups treated with Ppa-containing nanoformulations. During the entire course, the mice tumor volumes were monitored every other day, and they were persistently increased in the control group. In contrast, the tumor growth was restrained after the first injection of HH-PP and irradiation. The therapeutic effect of HH-PP was maintained until the experiment was completed (Fig. 7B). Although the mice tumor volumes were reduced to some degrees in other treatment groups compared to the mice injected with saline as a control, the degree of reduction in tumor volumes in these treatment groups was lower than that in the HH-PP + L-treated group. The tumor volume was used to determine the endpoint of the animal experiment. Mice were anesthetized and executed when the tumor volume in the mice injected with saline grew to larger than 1500 mm^3. At the end of the experiment, tumors were harvested for measuring the tumor weight and calculating the TGI. The tumor weight was 0.21 ± 0.02 g in the HH-PP + L-treated group, while it was 1.57 ± 0.11 g in the control group (Fig. 7C, Supporting Information Table S9). The TGI in the treatment groups varied from 38.89% to 86.63%, and the highest TGI was seen after treatment with HH-PP + L (Fig. 7D). These results confirmed synergistic anti-tumor effects of HH-PP + L (Fig. 7C−E).

Anti-tumor potency was further evaluated *in vivo* through tumor immunohistochemistry studies, including cell death, cell proliferation, and tumor angiogenesis. TUNEL staining was widely applied to various cell death modes, such as pyroptosis and ferroptosis, although it was initially invented for apoptosis investigation. The images confirmed a large number of TUNEL-positive cells or dead cells in the HH-PP + L-treated group. The signal of Ki67, a cell proliferation marker, in the tumor tissue suggested that cell proliferation was suppressed in the groups treated with HH-Ppa + L, HH-PP, and HH-PP + L. The highest level of restraining tumor cell proliferation was seen in the HH-PP + L-treated group. The images of CD31, a marker of new blood vessel formation, confirmed the lowest density of blood vessels in the tumor tissue after treatment with HH-PP + L (Fig. 7F and Supporting Information Fig. S39). All these results confirmed that HH-PP + L could exert an excellent anti-tumor effect *in vivo*.

The safety of these nanoformulations was also evaluated both *in vitro* and *in vivo*. The hemolytic assay was conducted by mixing 10% of red blood cells in PBS and different concentrations of nanoformulations. The hemolysis rates of HH-PTX and HH-Ppa were lower than 4%, and that of the assembled nanoformulations HH-PP were lower than 1% (Supporting Information Fig. S40 and Supporting Information Table S10). The mice's body weight was monitored during the entire experimental period to analyze the systemic toxicity of HH-PP, and the results showed there were no statistical differences in the body weight among all experimental groups (Supporting Information Fig. S41A). Besides, the mice's serum was collected for blood chemistry tests. The levels of the biochemistry parameters, including alanine transaminase (ALT), aspartate transaminase (AST), creatine kinase (CK), creatinine (CREA), and UREA in the peripheral blood of the treated mice were equivalent to those in the control mice, indicating that the treatment with HH-PP had a negligible effect on the function of the liver, heart, and kidney (Fig. 7G). The main organs of the mice were harvested, weighed, and stained with H&E at the end of the experiment. There were no statistical differences in the weights of main organs except spleen in all treatment groups compared to the control group (Fig. S41B−S41E). The spleens of tumor-bearing mice were enlarged, but they returned to a normal size following treatment with HH-PP + L (Fig. S41F), suggesting that HH-PP + L treatment may improve the overall health of the mice after tumor suppression. H&E staining images revealed no visible abnormal morphologies in all treatment groups (Supporting Information Fig. S42). Therefore, HH-PP has a great biosafety profile and can be readily transitioned into clinical studies.

4. Conclusions

We successfully synthesized two heparin-based graft polymers (HH-PTX and HH-Ppa) through RAFT polymerization and co-assembled them into HH-PP as a combinational nanomedicine for delivering Ppa and PTX. HH-PP displayed excellent stability in the simulated physiological environment *in vitro*. The pharmacokinetic analysis showed that ^{Rox}HH-PP prolonged the circulation time and increased the AUC of HH-Ppa and ^{Rox}HH-PTX. The live *in-vivo* images supported that HH-PP exhibited pronounced targeting of tumor cells and enhanced infiltration in tumor tissues. Following treatment with HH-PP and laser irradiation, ferroptosis was induced in tumor cells by disrupting lipid homeostasis, as evidenced by significant oxidation of lipid metabolites. Notably, the lipid peroxidation was amplified by the breakdown of LDs and TAG degradation, which further enhanced ferroptosis. After ferroptosis of tumor cells triggered by HH-PP + L, its anti-tumor effect was reinforced by activating immune responses, including DAMPs release, DCs maturation, and CTL proliferation. Importantly, HH-PP displayed a high biosafety profile by performing hemolytic assays and biochemistry tests, monitoring the mice's body weight, and staining major organs after harvest. Therefore, a novel and promising strategy has been demonstrated to induce ferroptosis of tumor cells *via* targeting the vulnerability of lipid metabolism by an intelligent drug delivery system, and its anti-tumor effect could be enhanced through immunology activation.

Acknowledgments

This work was financially supported by the National Key Research and Development Program of China (2023ZD0502304, 2023YFB3810004, 2022YFC2009900), Natural Science Foundation of China (32271445, 52073193), Department of Science and Technology of Sichuan Province (2024NSFJQ0050, China),

National Guidance Fund on Developing Local Science and Technology for Sichuan Province (2023ZYD0167, China), 1·3·5 project for disciplines of excellence, West China Hospital, Sichuan University (ZYGD23026, China).

We thank Hongying Chen, Dan Li, Cong Li, Jian Yang, Xuemei Chen, Yan Wang, Xiangyi Ren, Lei Wu, Yaping Wu, Zhengju Chen, Fengfeng Chen, and Shiqing Fu (Research Core Facility, West China Hospital, Sichuan University) for their help in confocal imaging studies, flow cytometry, and animal experiments. We thank Li Li, Fei Chen, Chunjuan Bao, and Yang Deng (Institute of Clinical Pathology, West China Hospital, Sichuan University) for processing histological staining. The authors thank Luolan Gui, Lu Zhang, and Wen Zheng (Metabolomics and Proteomics Technology Platform, West China Hospital, Sichuan University) for processing lipidomics analysis and LC−MS/MS quantification. We thank Qipu Feng (Animal Experiment Center, West China Hospital, Sichuan University) for animal model construction. We also thank Shanling Wang for her help with TEM images (Analytical & Testing Center of Sichuan University).

Author contributions

Ling Lin, Zaixiang Fang, Qiyong Gong, Kui Luo, and Jing Jing designed the research. Ling Lin and Zaixiang Fang carried out the experiments and performed data analysis. Yiwei Liu, Guohao Liu, Zhiqian Li, Xiaoding Shen, Hemi Kang, and Jingyao Zhang participated in some of the experiments. Zhiqian Li provided experimental drugs and quality control. Ling Lin, Zaixiang Fang, Dayi Pan, and Yunkun Li wrote the manuscript. Qiyong Gong, Kui Luo, and Jing Jing revised the manuscript. All of the authors have read and approved the final manuscript.

Conflicts of interest

The authors have no conflicts of interest to declare.

Appendix A. Supporting information

Supporting information to this article can be found online at https://doi.org/10.1016/j.apsb.2025.03.016.

References

1. Lei G, Zhuang L, Gan BY. The roles of ferroptosis in cancer: tumor suppression, tumor microenvironment, and therapeutic interventions. *Cancer Cell* 2024;**42**:513−34.
2. Newton K, Strasser A, Kayagaki N, Dixit VM. Cell death. *Cell* 2024; **187**:235−56.
3. Stockwell BR. Ferroptosis turns 10: emerging mechanisms, physiological functions, and therapeutic applications. *Cell* 2022;**185**: 2401−21.
4. Zhang C, Liu XY, Jin SD, Chen Y, Guo RH. Ferroptosis in cancer therapy: a novel approach to reversing drug resistance. *Mol Cancer* 2022;**21**:47.
5. Li PY, Lin QH, Sun SY, Yang N, Xia Y, Cao SJ, et al. Inhibition of cannabinoid receptor type 1 sensitizes triple-negative breast cancer cells to ferroptosis *via* regulating fatty acid metabolism. *Cell Death Dis* 2022;**13**:808−23.
6. Li J, He DJ, Li SC, Xiao J, Zhu ZY. Ferroptosis: the emerging player in remodeling triple-negative breast cancer. *Front Immunol* 2023;**14**: 1284057.
7. Hassannia B, Vandenabeele P, Berghe TV. Targeting ferroptosis to iron out cancer. *Cancer Cell* 2019;**35**:830−49.
8. Nong C, Guan PB, Li L, Zhang HY, Hu HB. Tumor immunotherapy: mechanisms and clinical applications. *MedComm Oncol* 2022;**1**:e8.
9. Li XR, Li YW, Tuerxun H, Zhao YX, Liu XY, Zhao YG. Firing up "cold" tumors: ferroptosis causes immune activation by improving T cell infiltration. *Biomed Pharmacother* 2024;**179**:117298−307.
10. Galassi C, Chan TA, Vitale I, Galluzzi L. The hallmarks of cancer immune evasion. *Cancer Cell* 2024;**42**:1825−63.
11. Hassannia B, Vandenabeele P, Berghe TV. Targeting ferroptosis as a vulnerability in cancer. *Nat Rev Cancer* 2022;**22**:381−96.
12. Koeberle SC, Kipp AP, Stuppner H, Koeberle A. Ferroptosis-modulating small molecules for targeting drug-resistant cancer: challenges and opportunities in manipulating redox signaling. *Med Res Rev* 2023; **43**:614−82.
13. Zheng JS, Conrad M. The metabolic underpinnings of ferroptosis. *Cell Metab* 2020;**32**:920−37.
14. Zhang XD, Liu ZY, Wang MS, Guo YX, Wang XK, Luo K, et al. Mechanisms and regulations of ferroptosis. *Front Immunol* 2023;**14**: 1269451-66.
15. Liu JY, Bai YN, Li YG, Li XL, Luo K. Reprogramming the immunosuppressive tumor microenvironment through nanomedicine: an immunometabolism perspective. *EBioMedicine* 2024;**107**:105301.
16. Diao JD, Jia YY, Dai EY, Liu J, Kang R, Tang DL, et al. Ferroptotic therapy in cancer: benefits, side effects, and risks. *Mol Cancer* 2024; **23**:89−101.
17. Zhang J, Zhang SJ, Liu ML, Yang Z, Huang R. Research progress on ferroptosis and nanotechnology-based treatment in triple-negative breast cancer. *Breast Cancer* 2024;**16**:347−58.
18. Song G, Li MH, Fan SM, Qin MM, Shao B, Dai WB, et al. Boosting synergism of chemo- and immuno-therapies *via* switching paclitaxel-induced apoptosis to mevalonate metabolism-triggered ferroptosis by bisphosphonate coordination lipid nanogranules. *Acta Pharm Sin B* 2024;**14**:836−53.
19. Zhang BB, Liu H, Wang YF, Zhang Y. ROS-responsive and self-catalytic nanocarriers for a combination of chemotherapy and reinforced ferroptosis against breast cancer. *ACS Biomater Sci Eng* 2024; **10**:6352−62.
20. Wen YY, Li KM, Ni MG, Jiang H, Wu HS, Yu Q, et al. Dendritic polylysine with paclitaxel and triptolide codelivery for enhanced cancer ferroptosis through the accumulation of ROS. *ACS Appl Mater Inter* 2024;**16**:20143−56.
21. Yu L, Liu Z, Xu W, Jin K, Liu JL, Zhu XH, et al. Towards overcoming obstacles of type II photodynamic therapy: endogenous production of light, photosensitizer, and oxygen. *Acta Pharm Sin B* 2024;**14**:1111−31.
22. Kang WR, Liu YW, Wang WP. Light-responsive nanomedicine for cancer immunotherapy. *Acta Pharm Sin B* 2023;**13**:2346−68.
23. Yan MM, Wu S, Wang YH, Liang MH, Wang MB, Hu WT, et al. Recent progress of supramolecular chemotherapy based on host−-guest interactions. *Adv Mater* 2024;**36**:2304249−81.
24. Li HN, Gong QY, Luo K. Biomarker-driven molecular imaging probes in radiotherapy. *Theranostics* 2024;**14**:4127−46.
25. Zhou Q, Xiang JJ, Qiu NS, Wang YC, Piao Y, Shao SQ, et al. Tumor abnormality-oriented nanomedicine design. *Chem Rev* 2023;**123**: 10920−89.
26. Huang XZ, He T, Liang XQ, Xiang ZZ, Liu C, Zhou SY, et al. Advances and applications of nanoparticles in cancer therapy. *MedComm Oncol* 2024;**3**:e67.
27. Liu JY, Li XL, Li YG, Gong QY, Luo K. Metformin-based nanomedicines for reprogramming tumor immune microenvironment. *Theranostics* 2025;**15**:993−1016.
28. Whitelock JM, Iozzo RV. Heparan Sulfate: a complex polymer charged with biological activity. *Chem Rev* 2005;**105**:2745−64.
29. Wang PP, Chi LL, Zhang ZQ, Zhao HM, Zhang FM, Linhardt RJ. Heparin: an old drug for new clinical applications. *Carbohydr Polym* 2022;**295**:119818.
30. Semsarilar M, Perrier S. 'Green' reversible addition-fragmentation chain-transfer (RAFT) polymerization. *Nat Chem* 2010;**2**:811−20.
31. Wu YH, Li FN, Zhang XQ, Li ZQ, Zhang QF, Wang WJ, et al. Tumor microenvironment-responsive PEGylated heparin-pyropheophorbide-a

nanoconjugates for photodynamic therapy. *Carbohydr Polym* 2021; **255**:117490.
32. Kopeček J. Hydrophilic biomaterials: from crosslinked and self-assembled hydrogels to polymer-drug conjugates and drug-free macromolecular therapeutics. *J Control Release* 2024;**373**:1−22.
33. Li HN, Feng Y, Luo Q, Li ZQ, Li X, Gan HT, et al. Stimuli-activatable nanomedicine meets cancer theranostics. *Theranostics* 2023;**13**: 5386−417.
34. Anh T, Mostafa A, Rao ZG, Pace S, Schwaiger S, Kretzer C, et al. From Vietnamese plants to a biflavonoid that relieves inflammation by triggering the lipid mediator class switch to resolution. *Acta Pharm Sin B* 2021;**11**:1629−47.
35. Ai XZ, Wang D, Honko A, Duan YO, Gavrish I, Fang RH, et al. Surface glycan modification of cellular nanosponges to promote SARS-CoV-2 inhibition. *J Am Chem Soc* 2021;**143**:17615−21.
36. Gu L, Duan ZY, Chen XT, Li XL, Luo Q, Bhamra A, et al. A transformable amphiphilic and block polymer−dendron conjugate for enhanced tumor penetration and retention with cellular homeostasis perturbation *via* membrane flow. *Adv Mater* 2022;**34**:2200048.
37. Fang ZX, Lin L, Li ZQ, Gu L, Pan DY, Li YK, et al. Stimuli-responsive heparin-drug conjugates co-assembled into stable nanomedicines for cancer therapy. *Acta Biomater* 2023;**164**:422−34.
38. Kadhem Z, Alkafeef S, Benov L. Singlet oxygen detection *in vivo* is hindered by nonspecific SOSG staining. *Sci Rep* 2024;**14**:20669.
39. Yan L, Liu Y, Ma XF, Hou D, Zhang YH, Sun Y, et al. Triclabendazole induces pyroptosis by activating caspase-3 to cleave GSDME in breast cancer cells. *Front Pharmacol* 2021;**12**:670081.
40. Wu LS, Bai SM, Huang J, Cui GH, Li QJ, Wang JS, et al. Nigericin boosts anti-tumor immune response *via* inducing pyroptosis in triple-negative breast cancer. *Cancers* 2023;**15**:3221−38.
41. Li YM, Ouyang Q, Chen W, Liu K, Zhang B, Yao JY, et al. An iron-dependent form of non-canonical ferroptosis induced by labile iron. *Sci China Life Sci* 2022;**66**:516−27.
42. Galluzzi L, Vitale I, Aaronson SA, Abrams JM, Adam D, Agostinis P, et al. Molecular mechanisms of cell death: recommendations of the nomenclature committee on cell death 2018. *Cell Death Differ* 2018; **25**:486−541.
43. Wang X, Hua P, He CW, Chen MW. Non-apoptotic cell death-based cancer therapy: molecular mechanism, pharmacological modulators, and nanomedicine. *Acta Pharm Sin B* 2022;**12**:3567−93.
44. Dixon SJ, Olzmann JA. The cell biology of ferroptosis. *Nat Rev Mol Cell Biol* 2024;**25**:424−42.
45. Du A, Wang Z, Huang TD, Xue S, Jiang C, Qiu GT, et al. Fatty acids in cancer: metabolic functions and potential treatment. *MedComm Oncol* 2023;**2**:e25.
46. Jin Y, Tan YJ, Wu J, Ren ZQ. Lipid droplets: a cellular organelle vital in cancer cells. *Cel Death Discov* 2023;**9**:254−63.
47. Alzeibak R, Mishchenko TA, Shilyagina NY, Balalaeva IV, Vedunova MV, Krysko DV. Targeting immunogenic cancer cell death by photodynamic therapy: past, present and future. *Immunother Cancer* 2021;**9**:e001926.
48. Deng W, Shang HJ, Tong YH, Liu X, Huang Q, He Y, et al. The application of nanoparticles-based ferroptosis, pyroptosis and autophagy in cancer immunotherapy. *J Nanobiotechnol* 2024;**22**:97−139.